Catena 167 (2018) 28–43

Contents lists available at ScienceDirect

Catena

journal homepage: www.elsevier.com/locate/catena

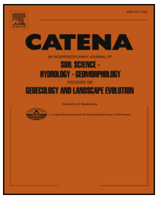

Global climate teleconnection with rainfall erosivity in South Korea

Jai Hong Lee[a,*], Joon-hak Lee[b], Pierre Y. Julien[a]

[a] *Department of Civil and Environmental Engineering, Colorado State University, Fort Collins, CO 80523, USA*
[b] *Department of Civil and Environmental Engineering, Korea Military Academy, Seoul 01805, South Korea*

ARTICLE INFO

Keywords:
Rainfall erosivity
Soil erosion
Teleconnection
El Niño-Southern Oscillation

ABSTRACT

Rainfall Erosivity Index (REI) defined as the product of rainfall kinetic energy and rainfall intensity is a well-known hydrologic indicator of the potential risk of soil erosion. Global and regional scale climatic teleconnections with REI variability over South Korea are examined. We calculate leading patterns of observed monthly REIs using the Empirical Orthogonal Teleconnection (EOT) and Function (EOF) decomposition techniques. Also we used monthly statistical analyses using cross-correlation and lag regression for the leading modes and global atmospheric circulation measurement in the Pacific and Indian Ocean. As a result, the northern inland mode is applicable during summer season and the southern coastal mode applies to fall-winter season. The temporal evolution of REI exhibits mostly increasing and depends on interdecadal oscillation patterns. The leading EOT modes explain more variance in REI than the EOF modes during warm and cold seasons. The findings from this study illustrate that the tropical ENSO forcing has the coherent association with fall and winter REI patterns, and the Indian Ocean dipole is identified as a driver for REI variability in November. The monsoon circulations over western North Pacific also exhibit significant negative correlation with the December modes. The September leading modes also show a positive correlation with the tropical cyclone activity. Leading patterns in September and November have predictability up to five month lead time from the tropical Pacific Sea Surface Temperatures (SSTs). In addition, predictability from the Pacific SSTs for above normal extreme value of REI is greater than that for below normal value in winter. In conclusion, South Korea experiences climatic teleconnection between the large scale climate indices and mid-latitude hydrologic variables.

1. Introduction

South Korea experiences spatial and temporal variability of climatic and hydrologic variables to a large degree. This spatiotemporal variability is in association with fluctuations of various global-regional scale climate indices (CIs), such as the El Niño–Southern Oscillation, Indian Ocean dipole, western North Pacific monsoon, and tropical cyclone activity. Classically, a climate index is defined as a diagnostic quantity used to characterize the state and change in the climate system with average state of the atmosphere over a long period, i.e., months and years, and to describe an aspect of a geophysical system such as a circulation pattern. These large scale climate indicators have been one of the most widely studied topics due to the fact that the extreme phases of the climatic impacts are usually related to major hydrologic extremes of floods and droughts in many regions all over the globe. In the global and regional scale studies, significant relationships have been reported between the large scale CIs and hydrologic parameters such as precipitation, streamflow, and rainfall erosivity in the tropics and extratropics.

The effects of the El Niño–Southern Oscillation (ENSO) on hydroclimatic variability on a global and regional scale are previously documented. Since the first investigation of Walker (1923) on the influence of the Southern Oscillation (SO) on rainfall fluctuations by Indian monsoon, recently many global scale studies focused on the evolution of ENSO cycle indicated noticeable climatic links between hydroclimatic parameters and the tropical ocean-atmospheric thermal forcing throughout the world. Bradley et al. (1987), Kiladis and Diaz (1989), and Ropelewski and Halpert (1989) pointed out notable ENSO-related signals with the identification of spatial structures and temporal cycles showing a statistically significant correlations between the tropical ENSO phenomena and precipitation variability throughout the various parts of the world. In addition, the regional scale works for low and middle latitude relating the remote ENSO cycle to hydroclimatic variations by Douglas and Englehart (1981), Shukla and Paolino (1983), Kahya and Dracup (1994), Rasmusson and Wallace (1983), Redmond and Koch (1991) and Price et al. (1998), revealed statistically significant correlation between regional precipitation and ENSO forcing. For midlatitude regions, the importance of the ENSO-streamflow

---

* Corresponding author.
E-mail address: june.lee@colostate.edu (J.H. Lee).

https://doi.org/10.1016/j.catena.2018.03.008
Received 26 June 2017; Received in revised form 16 February 2018; Accepted 8 March 2018

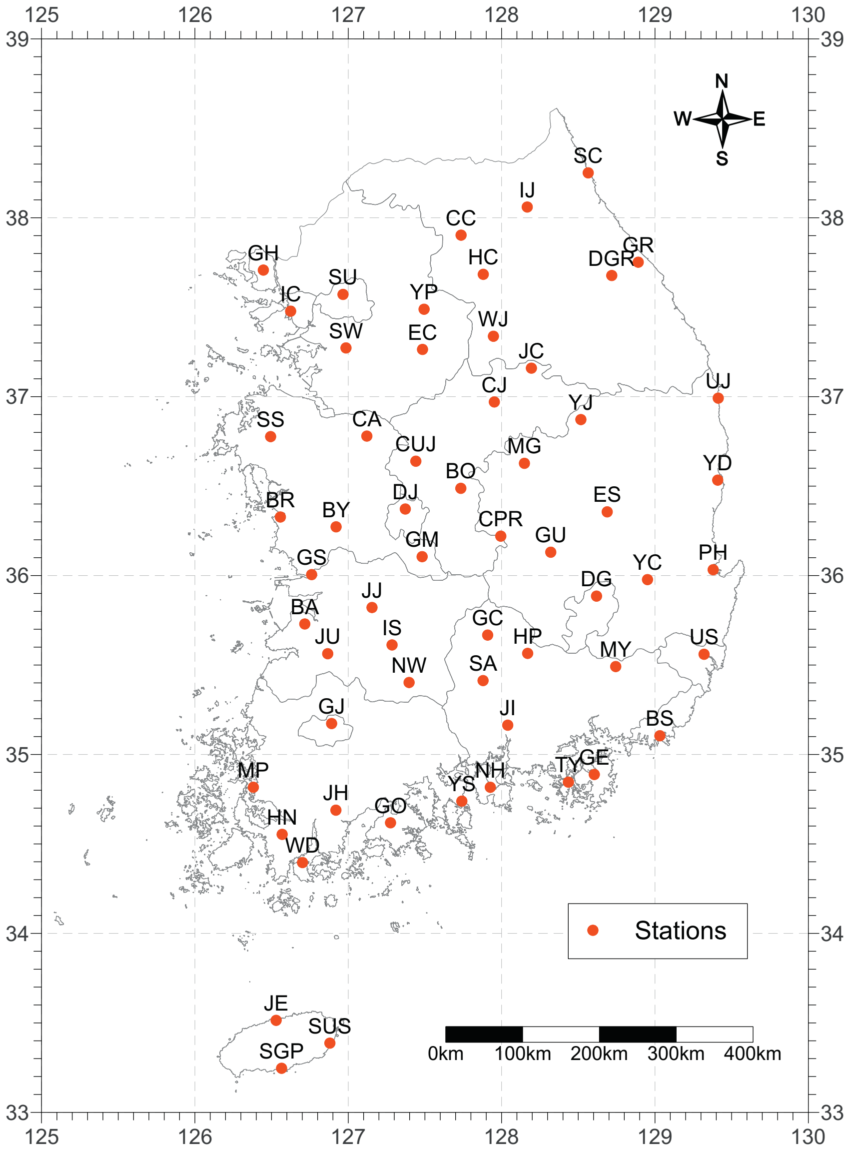

Fig. 1. Stations used for the REI indices.

relationships is emphasized in several studies. Cayan and Peterson (1989), Redmond and Koch (1991), Cayan and Webb (1992), and Diaz and Kiladis (1993) investigated the influence of North Pacific atmospheric circulation on streamflow in the western United States, and Kahya and Dracup (1994) diagnosed the impacts of ENSO on U.S. streamflow patterns from the perspective of extratropical teleconnections triggered by tropical sea surface temperature (SST) variation. In Asian regions, Chandimala and Zubair (2007) investigated the predictability of seasonal streamflow for the Kelani river basin in Sri Lanka associated with ENSO and SST anomalies using a correlation analysis and a principal component analysis.

Meanwhile, Indian Ocean dipole (IOD) has been considered as one of the key CIs of hydroclimatic variability in the Indian and Pacific rim countries. Some studies for IOD pointed out the distinct behavior of the IOD-related precipitation anomalies. Since Saji et al. (1999) reported a dipole mode of the Indian Ocean influencing on precipitation fluctuations, Ashok et al. (2001, 2003) revealed that notable climatic relationship exist between the IOD time series and the Indian monsoon precipitation variability as well as examined the remote response of Australian precipitation anomalies in winter to the IOD through an atmospheric general circulation model (AGCM). The monsoon and tropical cyclone activity could also be considered as a CI for hydroclimatic variability in the Indian and Pacific rim countries. Wang et al. (2008) performed a comparative analysis on pros and cons of 25 existing East Asian monsoon indicators from a viewpoint of interannual variabilities of precipitation and circulation, suggested a new index extracted by principal component analysis, and then stressed the important role of the mei-yu precipitation in quantifying the intensity of the East Asian monsoon activity.

Rainfall erosivity calculated by product of rainfall kinetic energy and rainfall intensity can be used a feasible hydrologic indicator of the potential risk of soil erosion due to climate change. Degradation of soil by water has been an important issue related agricultural productivity, forest and ecological conservation, and environmental problems in the world. The amount of rainfall has been used one of explainable parameters to predict the extent of degradation of soil, however, there have been limitations in explaining the reason why the strength of rainfall energy in two storms could be different if the amounts of rainfall are equal. Rainfall erosivity, which is known as input parameter of empirical models such as USLE or RUSLE for predicting long-term annual mean soil loss for arable land, is a numerical value which represents the erosion potential of soil erosion by water (Wischmeier and Smith, 1978; Renard et al., 1997). The result of soil loss using USLE model depends on the value of rainfall erosivity since the rainfall erosivity factor is

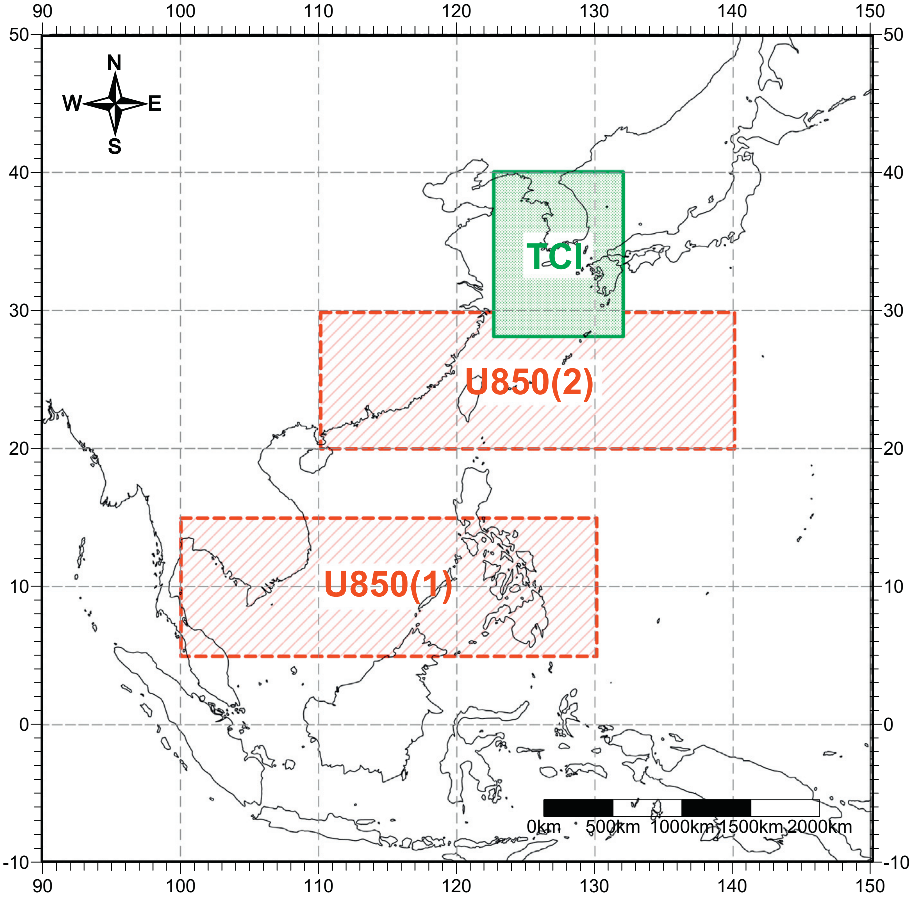

Fig. 2. Map of climate indices boundary.

directly correlated with the amounts of soil loss in USLE. Rainfall erosivity is a more accountable parameter to predict the amount of soil erosion than the amount of rainfall itself. Increasing of severe storms with high rainfall intensity accelerate soil erosion due to the fact that heavier rainfall have more energy to erode soil than lighter rain.

Numerical investigations on the impact of climate change on soil erosion through rainfall erosivity have been applied to sites all over the world (Panagos et al., 2017), including the USA (Nearing, 2001; Nearing et al., 2004; Biasutti and Seager, 2015; Hoomehr et al., 2015), China (Zhang et al., 2005), Japan (Shiono et al., 2013), Thailand (Plangoen et al., 2013; Plangoen and Babel, 2014), Australia (Yang et al., 2015), India (Mondal et al., 2016) and Iran (Mohammadi, 2015) and so on. Recent study by Panagos et al. (2017) used a regression approach to derive the distribution of rainfall erosivity in the future from climatic variables. Nearing (2001) reported that climate change can be expected to bring about the increase of soil loss by analyzing the variability of rainfall erosivity. Yang et al. (2003) insisted that climate change might significantly increase the potential risk of soil erosion in the future. Nearing et al. (2004) presented that rainfall erosivity was one of the important parameters to assess the potential climate change impacts on soil loss. Zhang et al. (2005) investigated the change of long-term annual mean rainfall erosivity and annual precipitation data according to two different climate change scenarios to predict the expected risk of soil erosion in the Yellow River Basin of China. Their result showed that the magnitude of rainfall erosivity increased significantly by climate change and the variability of rainfall erosivity included rainfall intensity was more sensitive than the variability of precipitation amount.

Several recent studies for South Korea have suggested statistically significant responses of hydroclimatic variables to the large scale CIs. Cha (2007) investigated the relationship between ENSO and IOD mode events and the impacts of these two phenomena on the precipitation of the Korean peninsula, and clearly indicated that the distribution of the Indian Ocean SST represents the Southern and Northern Oscillation in ENSO year, and Eastern and Western in IOD year with above normal precipitation departure in both summer and winter seasons. Lee and Julien (2017) revealed that two phases of the remote ENSO forcing are the dominant drivers of streamflow fluctuations over the Korean peninsula based on harmonic and lag correlation analysis. In the study on prediction of Korean precipitation variability using the downscaling super ensemble method, Kim et al. (2004) suggested that during winter the precipitation variability is correlated with the second EOF (Empirical Orthogonal Function) mode of sea lever pressure (SLP) over East Asia modulating moist flow from the WNP (Western North Pacific), and highlighted enhanced climatic response of the East Asian monsoon activity to precipitation anomalies in winter. Lee and Heo (2011) assumed that the outliers of rainfall erosivity in a particular year could be associated with severe storms under the influence of El Niño.

Many previous studies reported that they detected the spatial and temporal variability of rainfall erosivity by climate change, however, there have been limitations in explaining the cause of variability of rainfall erosivity related to various climatic parameters. In addition, despite these studies, the majority of studies with regional and global approaches concentrate on seasonal precipitation or streamflow, therefore there has been relatively little attention to the far reaching effects of climate indicators on hydrologic parameters such as Rainfall Erosivity Indices (REIs). Also, these studies have focused on mostly the global scale remote CIs such as El Niño–Southern Oscillation (ENSO) and Indian Ocean dipole (IOD) based on remote sources of large scale coupled ocean-atmospheric circulation on a global basis due to the fact

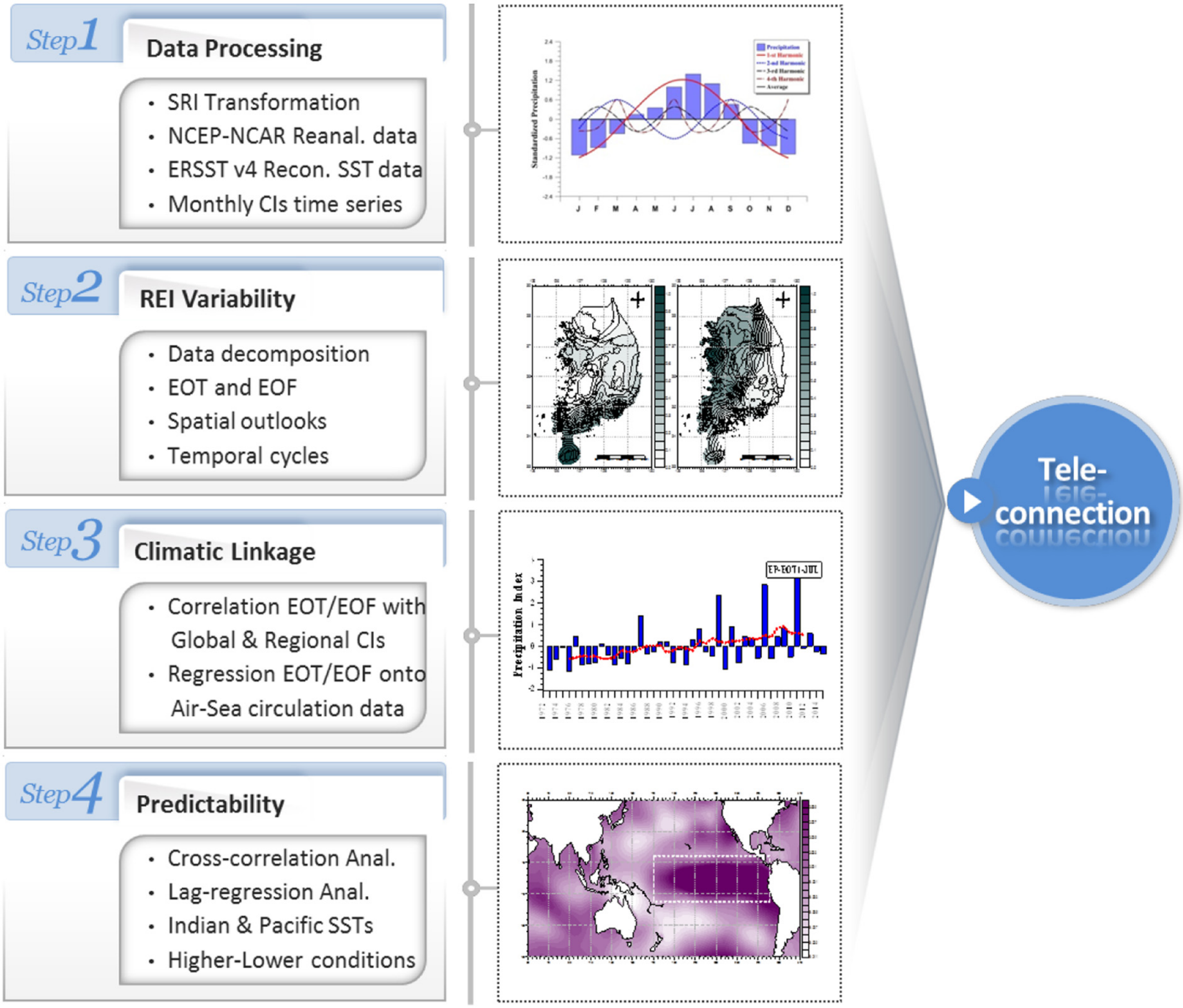

Fig. 3. Flowchart of the methodology.

that the regional scale local CIs, e.g., monsoon variability and tropical cyclone activity based on local synoptic-scale circulation patterns on a regional basis, are less distinct and influence less hydrologic extremes, e.g., floods and droughts, than the global scale CIs. Hence, there is no study in the literature concerning the climate impacts of both global and regional CIs on the REIs. However, the influence of climate indicators on the East Asian climatology is not limited to the global scale remote CIs, as well as, increasingly the potential researches of climatic teleconnections are asking for more information about the overall features of the hydrologic impacts modulated by various CIs. Thus, it is necessary to investigate systematically how both CIs affect the REI variability in the East Asian regions.

The present study mainly aims: (1) to investigate the spatial outlook and temporal cycle of REI anomalies over South Korea by means of Empirical Orthogonal Teleconnection (EOT) and Function (EOF) decomposition methods; (2) to identify significant climatic teleconnection between the previously extracted leading modes of REI variability and climate indicators with respect to the large scale climate fluctuations and regional synoptic circulation; and (3) to demonstrate predictability for REI patterns by sea surface temperature (SST), through the regression of the SST data on to the leading modes with varying lead times in order for the comparative interpretation of two opposite phases predictability, i.e., above and below normal conditions, in terms of magnitude and sign of the correlations.

2. Data and methods

2.1. Rainfall erosivity

Rainfall erosivity index is defined as the product of the total rainfall energy of heavy storms and the maximum 30 min of rainfall intensity (Wischmeier and Smith, 1978; Renard et al., 1997). The equation of REI is defined as:

$$E = \sum e\Delta\nu, \qquad REI = \sum_{k=1}^{m} (E)_k (I_{30})_k$$

where E means total rainfall energy, e is rainfall kinetic energy, $\Delta\nu$ is rainfall amount in individual storm events, I_{30} is maximum 30 min rainfall intensity, m is the number of the effective storm events, and REI is rainfall erosivity index. Several researchers attempted to calculate REIs using available precipitation data on a national scale in South Korea (Jung et al., 1998; Park et al., 2000). National Institute of Agricultural Sciences (NIAS) (2005) reported that the official value of annual average rainfall erosivity in South Korea was 4274 MJ mm/ha/h/yr as a follow-up to the studies by Jung et al. (1998) and Park et al. (2000) based on data before 1997. National Institute of Agricultural Sciences in South Korea developed the REI calculation program based on Visual Basic program (Park et al., 2011). This program adopted the rainfall kinetic equation by Wischmeier and Smith (1978) such as:

$$e = 210.3 + 89\log_{10} I \quad for\ I \le 7.6\ cm/h, \quad e = 289 \quad for\ I > 7.6\ cm/h$$

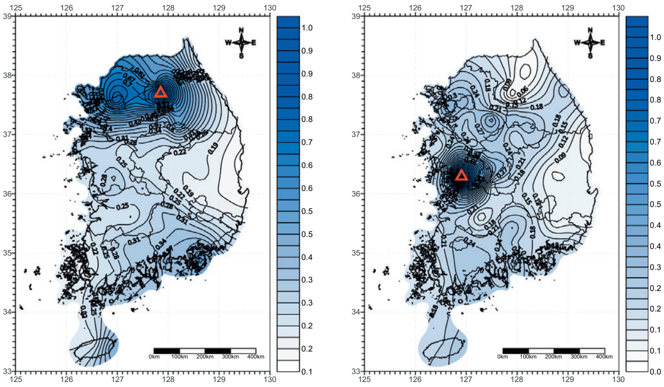

(a) JUL EOT-1

(b) JUL EOT-2

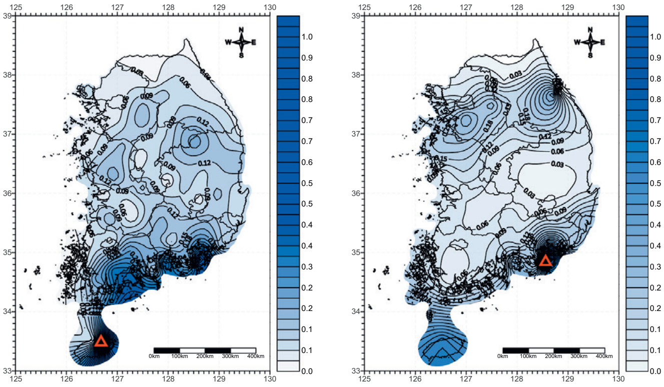

(c) NOV EOT-1

(d) NOV EOT-2

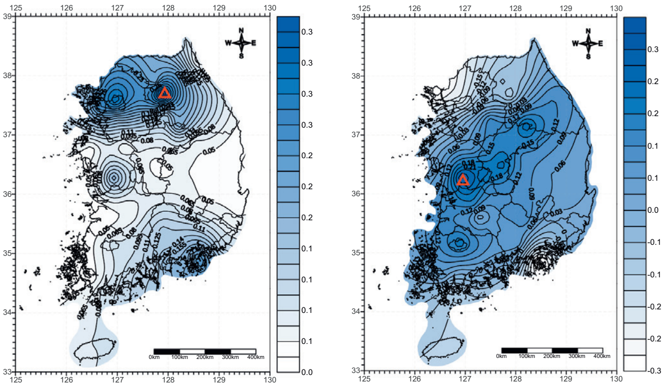

(e) JUL EOF-1

(f) JUL EOF-2

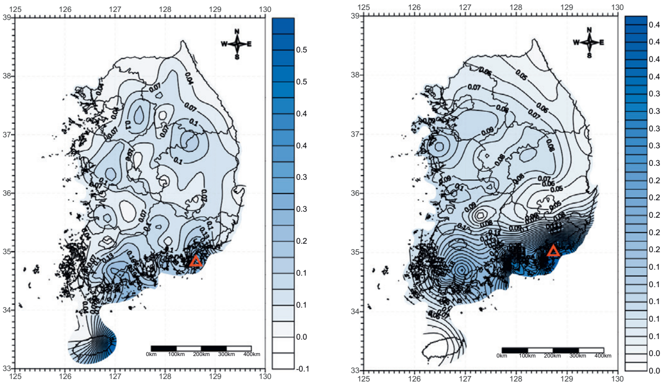

(g) NOV EOF-1

(h) NOV EOF-2

Fig. 4. Maps of the locations of base-points of each EOT (upper four panels) and EOF (lower four panels) and the correlations between EOT-EOF modes and time series at all other grid points for the first and second modes in July and November. Triangles indicate the base points.

where e means rainfall kinetic energy (Metric tonf/m/ha/cm), I indicates rainfall intensity (cm/h). If rainfall intensity is > 7.6 cm/h, the value of rainfall kinetic energy is 289 (Metric tonf/m/ha/cm). The calculated values were multiplied by 9.8 in order to match units in MJ mm/ha/h/yr. More recently, Risal et al. (2016) developed a web-based Erosivity estimation system (Web Erosivity Module, WERM) to compute rainfall erosivity factor using 10 min interval rainfall data (1997–2015) which have been used to determine yearly, monthly and event-based erosivity indices and such erosivity index values have been published for various weather stations in South Korea. WERM adopted RUSLE kinetic equation (Renard et al., 1997) as follows:

$$e = 0.119 + 0.0873 log_{10} I \quad for\ I \le 76mm/h, \qquad e = 0.283 \quad for\ I > 76mm/h$$

where e means rainfall kinetic energy (MJ mm/ha), I indicates rainfall intensity (mm/h). If rainfall intensity is > 76 mm/h, the value of rainfall kinetic energy is 0.283 (MJ mm/ha).

In this study, NIAS program based on hourly precipitation data transformed into I_{30} and Web Erosivity Module (WERM) were used over 58 stations for 1973–2015 in consideration of the temporal and spatial persistency as shown in Fig. 1. Based on the results from the correlation analyses for NIAS and WERM timeseries (2001–2008) showing good correlation coefficients up to 0.93, each monthly REI dataset was converted into Standardized Rainfall Erosivity Index (SRI) with respect to each month and station. Then, the combined SRI timeseries were decomposed into empirical orthogonal teleconnection (EOT) and function (EOF) modes.

2.2. *Climate indices*

For comparative analysis between large scale climate indicators and REI patterns, several CIs were applied in this present study. Taking into account both atmospheric and oceanic fluctuation, we employed the Oceanic Niño Index and the Multivariate ENSO Index as indicators for the tropical ENSO forcing, in addition to the Southern Oscillation Index which is widely used in atmospheric circulation analysis. The Oceanic Niño Index (ONI) is one of the main indicators for monitoring the tropical ENSO phenomena. The positive phase of extreme ENSO phenomena represents the condition that the ONI index exceeds +0.5, while the negative phase of ENSO events indicates the condition that the ONI index is lower than −0.5. The ONI is extracted by calculating the moving average values for consecutive 3-month SSTs (Sea Surface Temperatures) over the east-central Pacific Ocean, also known as Niño 3.4 index area of 120°–170°W and 5°S–5°N. The source of monthly ONI time series applied in this analysis is the dataset obtained from the National Oceanic Atmospheric Administration (NOAA)-Climate Prediction Center (CPC). The Multivariate ENSO Index (MEI) is derived from the leading modes calculated by unrotated decomposition technique for several air-sea variables over the tropical Pacific Ocean, such as SST, SLP (Sea Level Pressure), surface air temperature, total cloudiness fraction of the sky, and zonal-meridional surface wind. From the viewpoint of considering various factors associated with atmospheric and oceanic variation, the MEI may be considered as a better indicator representing relatively more information than other CIs. In this analysis, we employed the standardized bimonthly MEI values regularly updated by the Climate Diagnostic Center (CDC) since December 1949–January 1950. The Southern Oscillation Index (SOI), as an atmospheric pressure based climate indicator, is usually computed using Darwin-Tahiti mean sea lever pressure (MSLP) difference based on standardized index with zero mean and unit standard deviation. In the present analysis, we used the dataset of SOI calculated by the NOAA-Climate Prediction Center. Unlike the ONI and MEI, the positive phase of the SOI represents the La Niña-like conditions.

To examine the climatic relationship between the previously introduced CIs and the EOT/EOF modes for REI patterns, we employed

Table 1
Explained variance (VE) for the two leading modes of the monthly REI time series with the center of the leading mode, which is listed in parentheses: EC (east-coast mode), SC (south-coast mode), NL (north-inland mode), and ML (middle-inland mode). Triangles, inverted triangles, and circles indicate increasing trend, decreasing trend, and interdecadal patterns respectively.

Mode	JAN	FEB	MAR	APR	MAY	JUN	JUL	AUG	SEP	OCT	NOV	DEC
EOT modes												
EOT-1	0.43	0.67	0.62	0.66	0.63	0.48	0.45	0.30	0.43	0.36	0.64	0.60
	(SC) ●	(SC) ●	(SC) ●	(SC) ●	(SC)	(SC)▲	(NL)▲	(NL)	(SC)	(EC)	(SC)	(SC)
EOT-2	0.31	0.10	0.17	0.10	0.12	0.13	0.15	0.22	0.14	0.32	0.09	0.24
	(SC)	(SC)▼	(ML)	(SC) ●	(SC) ●	(SC)	(ML)	(EC)	(EC) ●	(SC)	(NL)	(SC)
EOF modes												
EOF-1	0.42	0.64	0.58	0.54	0.63	0.34	0.34	0.31	0.41	0.40	0.63	0.60
	(SC) ●	(SC) ●	(SC) ●	(SC)	(SC)	(SC)	(NL)▲	(NL)▲	(SC)▲	(EC)	(SC)	(SC)
EOF-2	0.29	0.10	0.20	0.14	0.11	0.18	0.13	0.20	0.16	0.29	0.09	0.24
	(SC)	(SC)▲	(SC) ●	(SC)▼	(SC) ●	(ML) ●	(ML) ●	(NL) ●	(SC) ●	(SC) ●	(NL)	(SC)

reconstructed SST and atmospheric circulation reanalysis field. As reconstructed SST data, the Extended Reconstructed SST (ERSST.v4) datasets (Huang et al., 2014) are used in this study. The ERSST is a global monthly SST dataset calculated based on the International Comprehensive Ocean and Atmosphere Dataset (ICOADS), which is widely used in global and regional scale studies. It is provided with global coverage on 2.0° × 2.0° grids through statistical analysis with the latest updated data and spans from January 1854 to the present. The global atmospheric circulation reanalysis dataset is based on the joint project of the National Centers for Environmental Prediction-National Center for Atmospheric Research (NCEP-NCAR). This dataset is a continually updated globally gridded dataset on 2.5° × 2.5° grids basis using state-of-the-art numerical modeling system for prediction and data assimilation with constantly updated observations. The monthly NCEP-NCAR reanalysis dataset is available for the period from 1948 to present.

Links between the leading modes and seasonal monsoon activity are investigated using the monsoon indices over western North Pacific, namely the western North Pacific monsoon index (WNPMI) (Fig. 2). From the methodological approach by Wang and Fan (1999), the WNPMI is calculated based on the difference between southern 850 hPa zonal winds designated as U850 (1) covering 5–15°N, 100–130°E and northern 850 hPa zonal winds designated as U850 (2) over 20–30°N, 110–140°E. The formal represents the intensity of the monsoon westerlies from Indochina Peninsula to the Philippines, while the latter indicates the magnitude of the easterlies over the southeastern part of the WNP subtropical anticyclone. The monthly Tropical Cyclone Index (TCI) quantifying the tropical cyclone activity is calculated based on the tropical cyclone tracks recorded by the IBTrACS (Knapp et al., 2010) and the National Typhoon Center (NTC) of Korea Meteorological Administration (KMA). For the period from 1973 through 2008, the TCI is obtained from the frequency of tropical cyclones passing through the index area as shown in Fig. 2.

2.3. Analysis

The method used in this analysis follows the empirical approach by Van den Dool et al. (2000) as outlined in schematic description of Fig. 3. The detailed procedures of the analysis method can be briefly summarized as follows. The first step is to convert the original data to monthly based time series, i.e., transformation of REI data into Standardized Rainfall Erosivity Index (SRI) with respect to each month and station. Then, the Empirical Orthogonal Teleconnection (EOT) and Function (EOF) decomposition techniques are performed for identification of spatiotemporal variability of REIs over South Korea. Finally, the cross correlation and linear regression analyses examine teleconnections between global and regional CIs and the leading modes. And the final step is to perform lag correlation approach using the regression of the SST data onto EOT/EOF modes with varying lead times in order for the comparative interpretation of two opposite phases predictability, i.e., above and below normal conditions, in terms of magnitude and sign of the correlations.

Prior to the EOT/EOF analyses to examine the CI-REI teleconnection, we converted the original data to the SRI formulated for effective assessment of wet and dry condition by McKee et al. (1993). The SRI calculating procedures following the approach of McKee et al. (1993) and Lee and Julien (2015) are outlined as follows: (1) The monthly observational data of 59 stations are transformed into the time series fitted to gamma distribution for each month; (2) The fitted frequency distribution is converted to cumulative distribution function (CDF) of the standard normal distribution based on equal-probability condition; (3) The final SRI dataset, which is subjected to the EOT/EOF processes, can be computed by means of the standard deviations obtained from the above CDF with zero mean and unit variance. The SRI is very straightforward to estimate due to the fact that the one variable is used as input data, as well as very easy to compare from a spatial and temporal viewpoint since the index is presented as dimensionless values. Furthermore, Guttman (1998) indicated that the above index is useful and conducive to statistical data process.

To investigate spatiotemporal patterns of REIs over South Korea, we employ the EOT decomposition technique reported by Van den Dool et al. (2000) with the classical analysis of the EOF. The EOT decomposition approach is similar to that of the EOF in terms of representing an objective method of selecting patterns that explain the maximum amount of variance in a data set. The difference between the two approaches is that the former is orthogonal in one direction of space or time, while the latter is orthogonal in two directions of space and time. The EOT spatiotemporal analysis decomposes the dataset into a set of orthogonal components, called EOT patterns. Due to the fact that the EOT decomposition technique is orthogonal in one direction of space or time, the EOT method provides more intuitive interpretation for resulting patterns. The first EOT spatial modes are obtained by finding the point with the highest sum in explained variance of all other points, which is designated as a base point by Van den Dool et al. (2000). Then, the time series of the base point is the first temporal modes of the REI patterns. The second EOT spatial modes are extracted by removing the influence of the base point on all other points using regression analysis for the dataset of the base point and all other points. From the reduced dataset, the second base point is identified by detecting the point explaining the most variance over the residual domain. For further modes, the successive data reduction is repeated for the residual domain decomposed by the preceding modes until the desired number of modes is detected. For example of the time series (SRI) of January over the entire period, we have a discrete space-time (s, t) dataset SRI(s, t), $1 \leq t \leq t_{max}$ and $1 \leq s \leq s_{max}$, where SRI denotes the monthly time series of Standardized Rainfall Erosivity Index (SRI) transformed from REI data with respect to each month and station. A stepwise linear regression is employed to extract EOT values, where both the predictands and predictors are SRI(s, t). We can search all s for that point

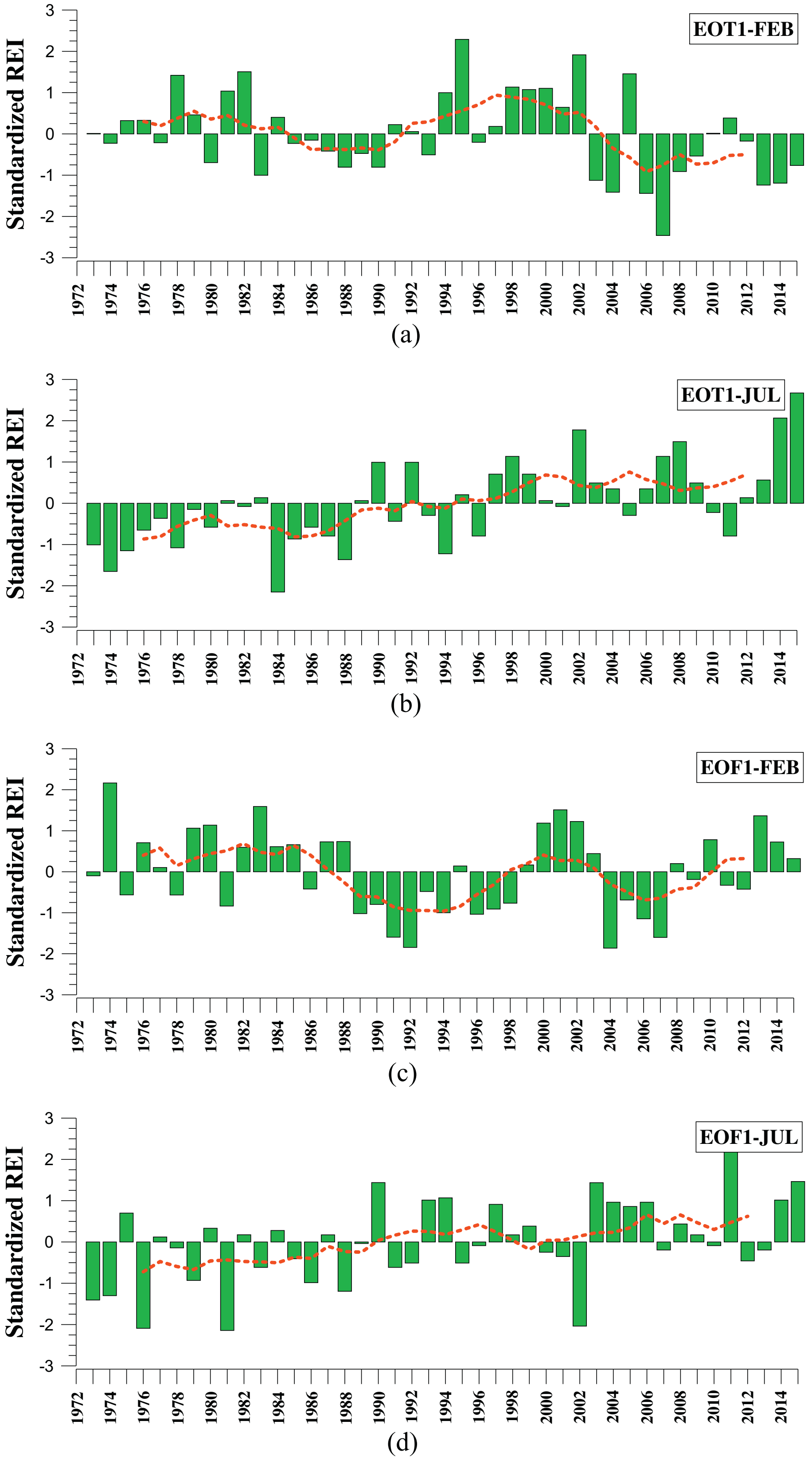

Fig. 5. Annual time series (bars) and their 7-year running means (thick lines) for the leading mode with inter-decadal (a, c) and increasing trend (b, d). The upper two panels are the temporal cycles for EOT modes and the lower two panels are those of EOF modes.

Table 2

Correlation coefficients of the two leading modes with climate indicators, ONI (Oceanic Niño Index), MEI (Multivariate ENSO Index), SOI (Southern Oscillation Index), IOD (Indian Ocean Index), WNPMI (Western North Pacific Monsoon Index), and TCI (Tropical Cyclone Index). An underlined bold indicates correlations that are statistically significant at the 5% level.

Mode	Monthly CIs for EOT modes						Monthly CIs for EOF modes					
	ONI	MEI	SOI	IOD	WNPMI	TCI	ONI	MEI	SOI	IOD	WNPMI	TCI
The 1-st mode												
AUG	0.18	0.24	−0.19	0.08	0.10	0.02	−0.07	−0.08	0.07	−0.08	0.10	0.01
SEP	**−0.35**	**−0.35**	**0.26**	−0.24	−0.14	**0.39**	−0.25	−0.25	0.25	−0.25	−0.02	**0.29**
OCT	−0.14	−0.17	0.05	−0.13	0.10	0.24	0.10	0.06	−0.08	0.06	0.24	0.05
NOV	**0.40**	**0.50**	**−0.51**	**0.48**	−0.09	−0.02	**0.45**	**0.51**	**−0.52**	**0.51**	−0.16	−0.10
DEC	**0.34**	**0.37**	**−0.40**	0.23	**−0.29**	–	0.25	0.25	**−0.29**	0.25	**−0.26**	–
The 2-nd mode												
AUG	−0.22	−0.22	0.22	−0.03	0.25	**−0.27**	0.25	0.19	−0.20	0.19	**0.30**	**0.28**
SEP	0.10	0.12	0.00	−0.09	−0.18	**−0.36**	−0.22	−0.18	0.16	−0.18	−0.17	0.08
OCT	**−0.41**	**−0.40**	**0.32**	**−0.30**	−0.17	**0.26**	**−0.41**	**−0.30**	0.12	**−0.30**	−0.09	0.51
NOV	−0.02	0.04	0.03	−0.05	0.15	−0.12	−0.15	−0.11	−0.07	−0.10	**0.29**	−0.06
DEC	0.25	0.21	−0.22	−0.17	−0.23	–	0.16	0.10	−0.06	0.12	−0.09	–

in space, namely a base point (sb), that explains the most of the variance at all other points including itself combined. What is explained by SRI(sb, t) is removed from SRI(s, t) by standard regression, and we can search the reduced data for the next most important point in space based on explained variance. Eventually we can obtain $\mathrm{SRI}(s, t) = \Sigma\alpha_n(t)\ e_n(s)$, where the $\alpha_n(t)$ are time series and the $e_n(s)$ are spatial patterns, and the summation is over mode $m = 1, \ldots, s_{\max}$. In this analysis, we also employed the revised EOT decomposition technique modified by Smith (2004), who demonstrated the base point selection based on the explained variance for the entire domain-weighted dataset instead of the highest sum in explained variance of all other points. Following the above procedure, the first and the second modes were obtained for monthly dataset in the period of 1973–2008 to investigate various REI fluctuations in different area of South Korea.

Following the approach by King et al. (2014), all correlation coefficients between the EOT/EOF modes and various CIs are calculated using Spearman's correlation analysis at the 5% significant level taking into account the fact that some CI time series may not feature normal distribution. Although the correlation analysis was performed by Spearman's rank test, the resultant correlation coefficients were in general agreement with those calculated by the commonly used Pearson's product method. The overall findings from correlation and regression analyses between all EOT/EOF modes and various CIs are described with correlation maps and regression maps.

3. Results and discussions

3.1. Spatio-temporal patterns of EOT/EOF

EOT/EOF modes were extracted from the REI time series for the period of 1973–2008. For spatial outlook of the REI patterns, correlation maps for each mode showing the highest value of explained variance for the entire domain-weighted REIs were plotted on a monthly basis. Values displayed in these maps are the correlation coefficients between the EOT/EOF time series in the base point with all other point time series. Each monthly leading mode has the most explained variance for the REIs and shows unipolar spatial patterns across South Korea. The spatial patterns of the base points and highest correlation values for each month reflect the climatological seasonal patterns in association with the influence of midlatitude weather systems around the Korean peninsula. Once the leading modes are identified, the next step is to remove their influence on the dataset, prior to repeating the whole procedure. This is done by using the results of linear regression of previously detected leading EOT/EOF time series onto each individual point value, and subtracting out that proportion of the REI signal explained by the first modes. Having removed the influence of the leading EOT/EOFs from the data, the analysis continues by finding that the point whose time series most closely matches the resultant residual time series. Fig. 4 show the resultant patterns for the EOT/EOF of July and December REI from the above analyses.

The base points of the first EOT/EOF modes show different locations with respect to months. The locations of base points for EOT modes are similar to those for EOF modes during the summer months, in the north and inland of South Korea. In the fall-winter months, the base points of leading EOTs have a tendency to shift southward but more so for those of EOF modes to the southernmost island. This is particularly clear in July (Fig. 4a, e) and November (Fig. 4c, g), where the base points of the leading EOT modes are located in northern central and southern coastal area, respectively. For all months, the centers of the leading modes are located in coastal area (37 modes) and inland area (11 modes). Since the overall lower-order EOT/EOF modes such as the third, forth, etc., modes show more variability in the locations of the base points, the results of the lower-order decomposition analyses were excluded. Locations of the base points represent that out of twenty four EOT/EOF modes, i.e., two modes for each of twelve months, 19/18 are identified as coastal mode and 5/6, inland mode as shown in Table 1. In detail, the coastal mode consists of south-coast mode (16/17) and east-coast mode (3/1) based on the center of leading mode, while inland mode comprises north-inland mode (3/4) and middle-inland mode (2/2). From the spatial findings of the above analyses, the spatial outlook of the leading modes represents northern inland mode for boreal summer season and southern coastal mode in winter season. In general, there is no consistent spatial homogeneity in both leading modes during the summer and winter seasons except for July EOF-2 mode with more widespread coherent patterns showing nationwide spatial homogeneity.

The total spatiotemporal variance related to the two leading modes varies with months and modes. Table 1 shows that the spatiotemporal variance related to each EOT/EOF mode is 0.30/0.31 to 0.67/0.64 for each first mode, while that for lower-order modes decreases to around 0.09 at the second modes for each month. Explained variance by the leading EOT modes is slightly larger than that by the first EOF modes in most months due to the fact that the former is more likely to feature homogeneities as opposed to the latter having less coherent variability (Van den Dool et al., 2000). Temporal cycles were identified for the two leading modes of EOT/EOF time series (Fig. 5). From the temporal findings of the above analyses, fifteen out of twenty four leading EOT modes exhibits noticeable pattern, which are 4 increasing trend, 1 decreasing trend, and 10 interdecadal patterns as shown in Table 1. The temporal cycles of the EOF time series show 10 noticeable trends, e.g., 2 increasing trend, 1 decreasing trend, and 7 interdecadal fluctuations. The temporal trends of leading modes in January and February are in

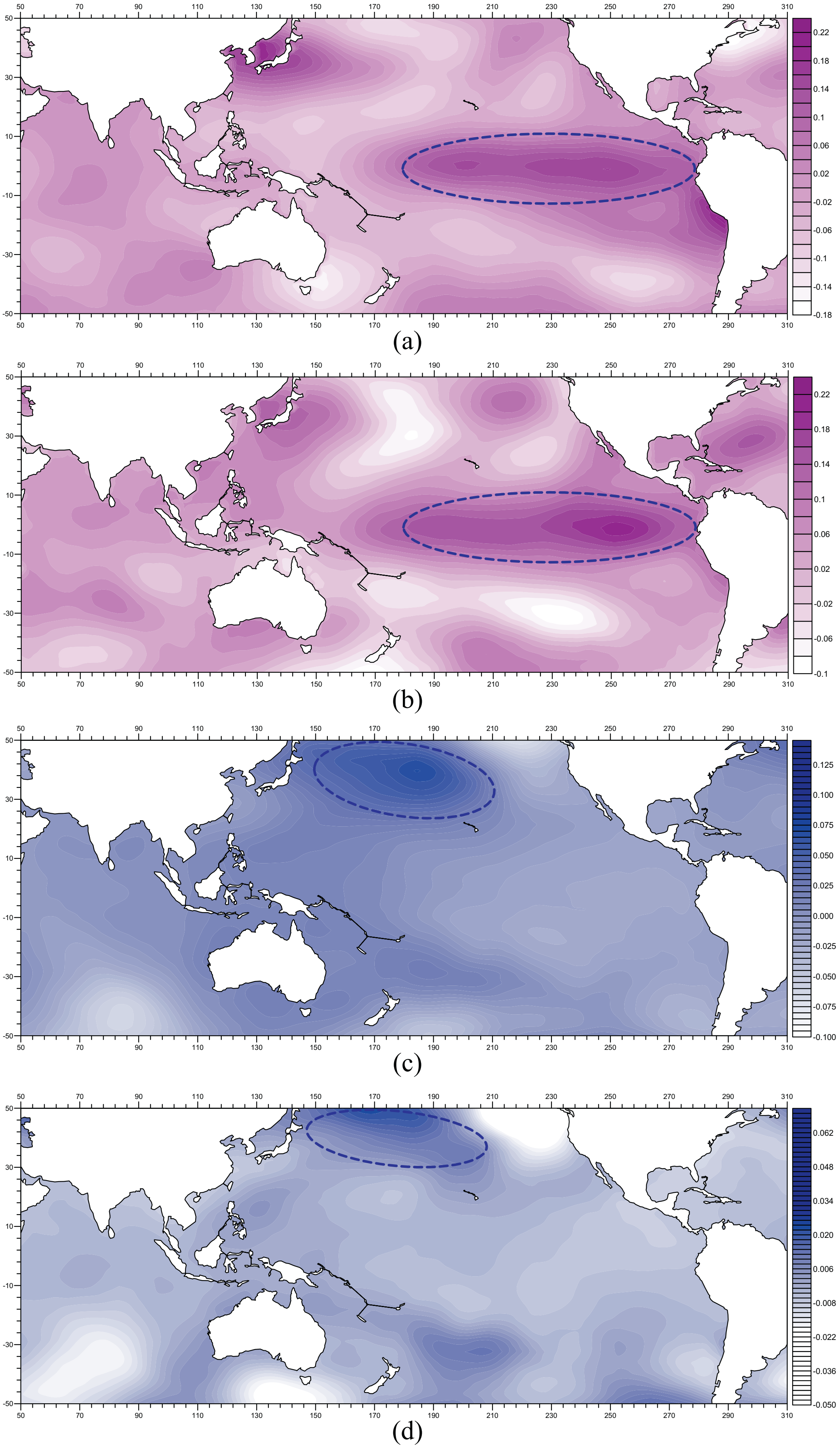

(caption on next page)

Fig. 6. Maps of SST (a)–(b) and MSLP (c)–(d) regressed on to November leading modes of EOT (upper) and EOF (lower) respectively. The values of each grid of the maps (a)–(b) are calculated using regression coefficients for Sea Surface Temperature (SST) of ERSST. v4 reconstructed field on the leading modes of EOT and EOF, and the values of the maps (c)–(d) are calculated using regression coefficients for Mean Sea Level Pressure (MSLP) of NCEP-NCAR reanalysis on the leading modes of EOT and EOF. The dashed lines indicated ENSO–like SST patterns which exhibits warmer SST anomalies over the central-eastern tropical Pacific (a)–(b) and ENSO-like SLP patterns of higher pressure in the western North Pacific (c)–(d).

Table 3

Cross-correlation coefficients of the leading modes with climate indicators. The bold, single underlined bold, and double underlined bold indicate correlations that are statistically significant at the 0.15, 0.10, and 0.05 level.

Mode	Monthly CIs for EOT modes							Monthly CIs for EOF modes						
	JUN	JUL	AUG	SEP	OCT	NOV	DEC	JUN	JUL	AUG	SEP	OCT	NOV	DEC
Lag modes for Oceanic Nino Index (ONI)														
AUG	0.22	0.18	0.18					-0.01	-0.06	-0.07				
SEP	**-0.31**	**-0.36**	**-0.36**	**-0.35**				-0.21	**-0.27**	**-0.26**	**-0.25**			
OCT	-0.17	-0.22	**-0.23**	-0.21	-0.14			0.00	-0.01	0.06	0.06	0.10		
NOV	**0.40**	**0.44**	**0.40**	**0.38**	**0.39**	**0.40**		**0.44**	**0.51**	**0.48**	**0.48**	**0.47**	**0.45**	
DEC	**0.34**	**0.39**	**0.39**	**0.38**	**0.36**	**0.32**	**0.34**	**0.27**	**0.32**	**0.32**	**0.32**	**0.28**	**0.23**	**0.25**
Lag modes for Multivariate ENSO Index (MEI)														
AUG	**0.26**	**0.23**	**0.24**					0.03	-0.03	-0.08				
SEP	**-0.30**	**-0.34**	**-0.34**	**-0.35**				-0.19	**-0.24**	**-0.24**	**-0.25**			
OCT	-0.19	-0.18	-0.18	-0.18	-0.17			-0.06	-0.03	0.05	0.05	0.06		
NOV	**0.28**	**0.34**	**0.33**	**0.41**	**0.50**	**0.50**		**0.34**	**0.41**	**0.39**	**0.42**	**0.51**	**0.51**	
DEC	**0.28**	**0.34**	**0.41**	**0.38**	**0.35**	**0.37**	**0.37**	**0.23**	**0.30**	**0.36**	**0.30**	**0.26**	**0.26**	**0.25**
Lag modes for Southern Oscillation Index (SOI)														
AUG	**-0.27**	-0.16	-0.19					0.01	0.09	0.07				
SEP	0.22	**0.31**	**0.38**	**0.26**				**0.26**	**0.25**	**0.36**	**0.25**			
OCT	**0.27**	-0.01	0.00	0.03	0.05			0.16	0.01	-0.20	-0.07	-0.08		
NOV	**-0.45**	**-0.35**	**-0.33**	**-0.45**	**-0.53**	**-0.51**		**-0.56**	**-0.44**	**-0.44**	**-0.56**	**-0.52**	**-0.52**	
DEC	-0.22	**-0.40**	**-0.49**	**-0.37**	**-0.35**	**-0.27**	**-0.40**	-0.17	**-0.35**	**-0.39**	**-0.29**	**-0.27**	-0.20	**-0.29**
Lag modes for Indian Ocean Dipole Index (IOD)														
AUG	0.01	-0.05	0.08					**-0.23**	**-0.33**	0.08				
SEP	**-0.27**	**-0.29**	**-0.26**	**-0.24**				**-0.23**	**-0.35**	**-0.26**	**-0.25**			
OCT	-0.14	-0.16	-0.14	-0.05	-0.13			-0.02	-0.03	0.02	0.08	0.06		
NOV	**-0.28**	-0.07	-0.01	0.06	0.12	**0.48**		-0.21	0.01	0.04	0.20	**0.24**	**0.51**	
DEC	0.03	0.16	0.21	**0.35**	**0.26**	**0.28**	**0.23**	0.06	0.14	0.14	**0.28**	0.20	0.21	0.25

agreement with the findings of the previous study by Kim et al. (2004) where the temporal cycles of the first mode over the Korean peninsula are observed to exhibit significant interdecadal trends in winter. The temporal evolution of the leading modes indicates increasing trends during summer season (July) and oscillation on mainly inter-decadal timescales for winter season (January and February). For the period of study, many leading modes have significant signals to a great extent throughout overall spatial domain of South Korea with large scale influence coverage. This implies that the hydrologic regimes associated with a common large scale circulation process dominate and drive spatiotemporal REI variability over South Korea.

3.2. Teleconnections between EOT/EOFs and CIs

For the purpose of investigating the far reaching effects of various CIs on REI variability across South Korea, the leading modes were correlated with several climate indices representing spatially and temporally significant variability such as ENSO and IOD. Table 2 shows the correlation coefficients between various CIs and EOT/EOF modes, where only EOT/EOF modes showing significant correlation were included. In addition, as shown in Fig. 6 regression maps for NCEP-NCAR reanalysis and ERSST. v4 reconstructed field were described depending on each mode. Many regression maps indicate notable signals consistent with the spatial patterns commonly reported in the hydroclimatic signals studies examined.

The correlation coefficients for each mode and ENSO indicator were calculated using the ONI, the MEI, and the SOI. As shown in Table 2, the ONI time series has the significant negative correlations with the leading EOTs in September, whereas the leading EOTs for November and December exhibit the positive correlation with the tropical Pacific SST. The MEI correlations similarly reflect the results of ONI-related EOT signals with mostly significant correlations showing transitional pattern from negative to positive. The SOI exhibits significant positive correlations with the leading EOTs during early fall season (September), while in the winter season (December) the first EOT shows the negative correlation with the SOI. In Table 2, the SST-related signal in association with ENSO is weaker in spring and early summer reflecting the fact that climatic links between the EOT modes and ENSO indices are not

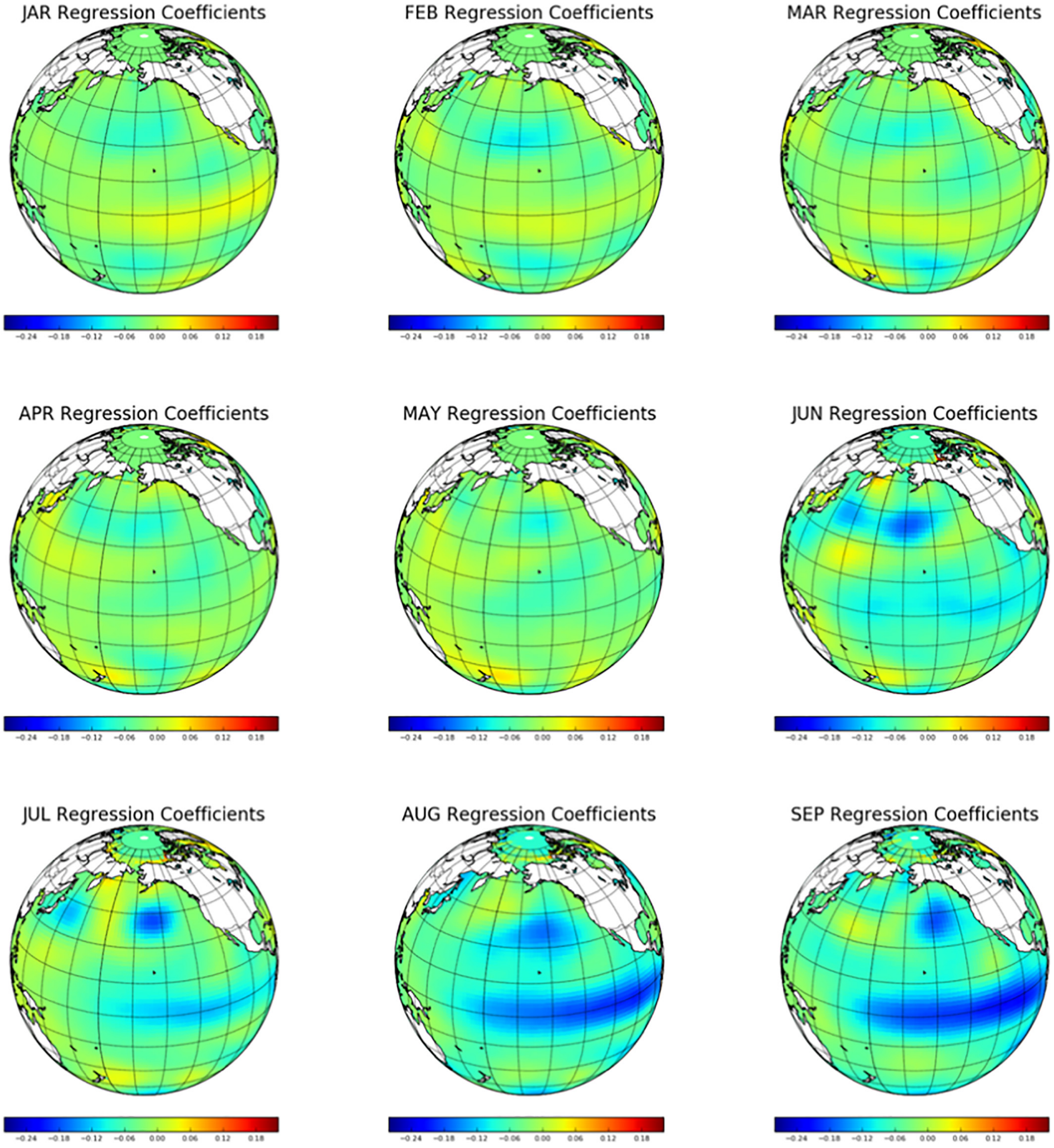

Fig. 7. Maps of SSTs of Lag-8 (January) to Lag-0 (September) regressed on to September leading mode. The values of each grid of the maps are calculated using regression coefficients for Sea Surface Temperature (SST) of ERSST. v4 reconstructed field on the leading modes.

significant at this time of year since the extreme ENSO phenomena are generally not yet fully mature phase or are already decay phase. In addition to the leading EOTs, the other lower-order EOT in some regions show relatively significant correlations in October. The findings from the above correlation analysis suggest that the El Niño (La Niña) events exert a controlling impact over above (below) normal REI in southern and inland of South Korean in general. The EOF modes also have significant correlations with ENSO indicators. The ONI, MEI, and SOI index show slightly lower correlation coefficients with the EOFs compared with the EOT modes, but both correlation results show a similar seasonal cycle.

The climatic linkages between the leading EOT/EOF modes and the ENSO indicators also can be identified through regression fields. Enhanced EOT/EOF modes are also attributed to the typical ENSO SST cycle which exhibits warmer SST anomalies over the central-eastern tropical Pacific (Fig. 6a and b). Above normal signals in many EOT/EOF modes are closely related to ENSO–like SST patterns. In addition to the tropical Pacific SST Pattern, regressing MSLP onto the leading modes

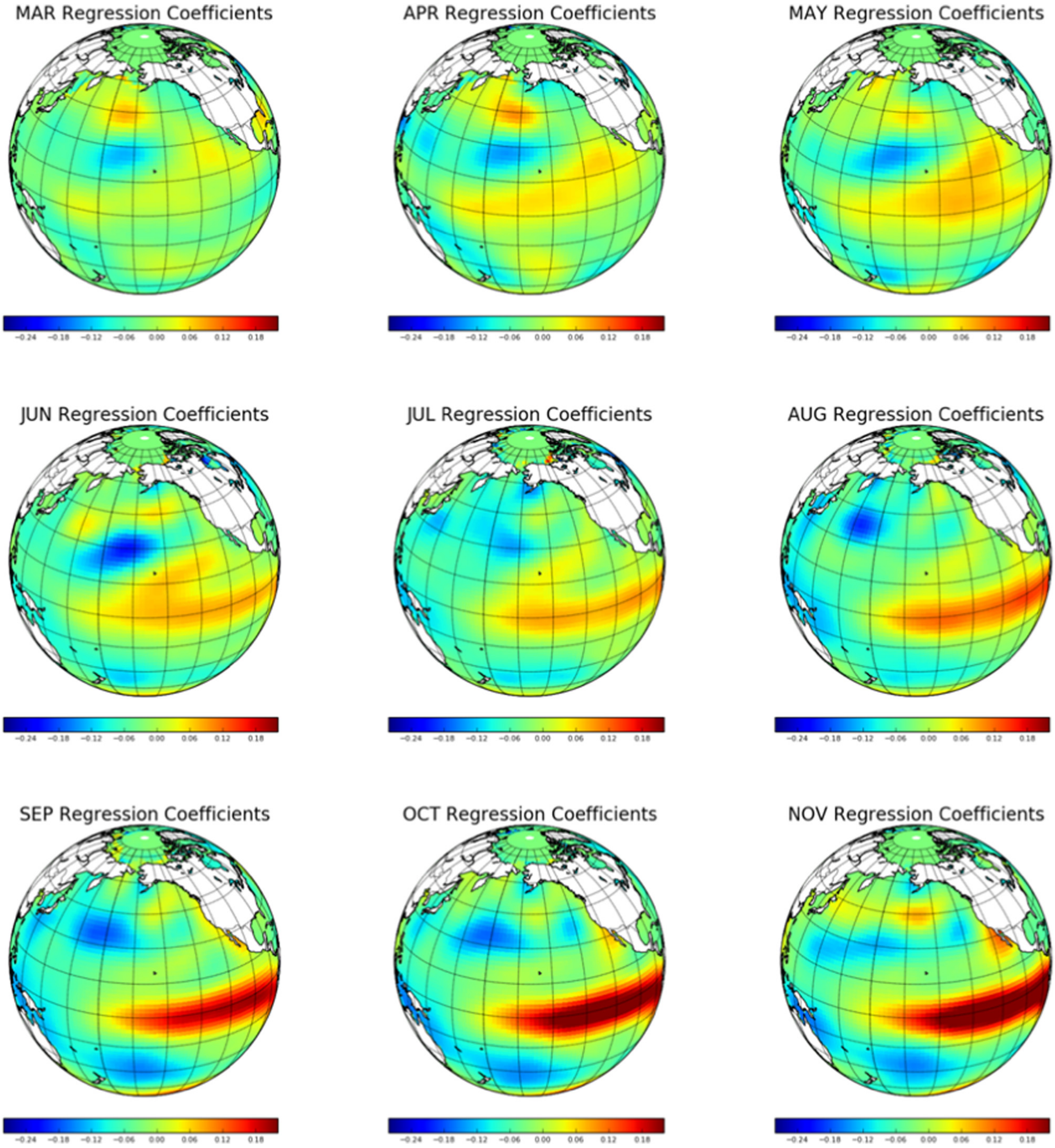

Fig. 8. As in Fig. 7, except for Lag-8 (March) to Lag-0 (November) regressed on to November leading mode.

(Fig. 6c and d) describes similar ENSO-like SLP patterns of higher pressure in the western North Pacific and lower pressure in the eastern North Pacific region. This reflects the Pacific-East Asian teleconnection (PEA) which represents the damping phases of East Asian winter monsoon induced by the western North pacific anticyclone and the warm phases over the eastern equatorial Pacific Ocean (Wang et al., 2000). This phase of the PEA teleconnection promotes variation of REI over South Korea during ENSO winter in particular.

The correlation coefficient of monsoon variability with each EOT/EOF mode was calculated for the WNPMI index. From the results of correlation analysis in Table 2, the leading EOTs for December exhibit the negative correlation with the monsoon variability over the WNP region. In the positive WNPMI phase, anomalous cyclones are reinforced in the WNP area due to the intensification of WNP monsoon trough, which is caused by the strengthening of westerlies over the U850 (1) region in Fig. 2 from the Philippine Sea to the Indochina peninsula and the enhancement of easterlies in the U850 (2) region over the southern flank of the WNP subtropical high. This positive WNPMI phase has an effect on lower than average REI anomaly in South Korea. The EOF modes also show similarly significant correlation with the monsoon variability. The monsoon indices show somewhat lower correlations with the EOT modes than those for EOF modes but exhibit a similar temporal pattern. The monthly TCI indices were calculated for the index area to the south part of the Korean peninsula (Fig. 2). Each TCI is correlated with the EOT/EOF modes for REI time series from May to November. Seven out of thirty two modes show the

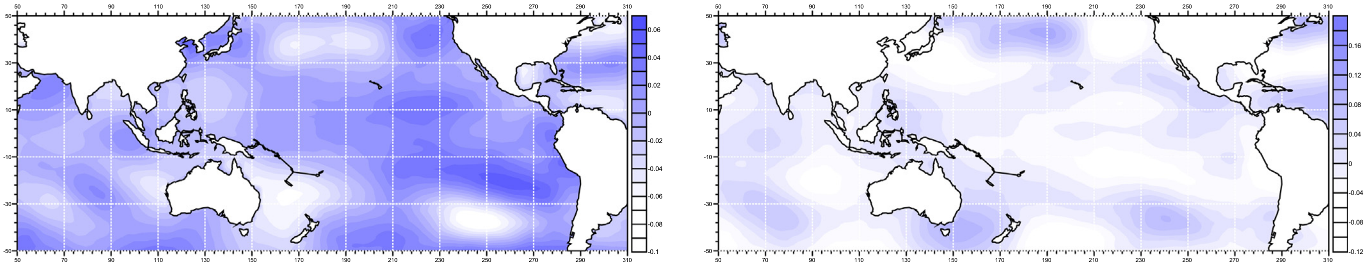

(a) MAR SST

(b) JUN SST

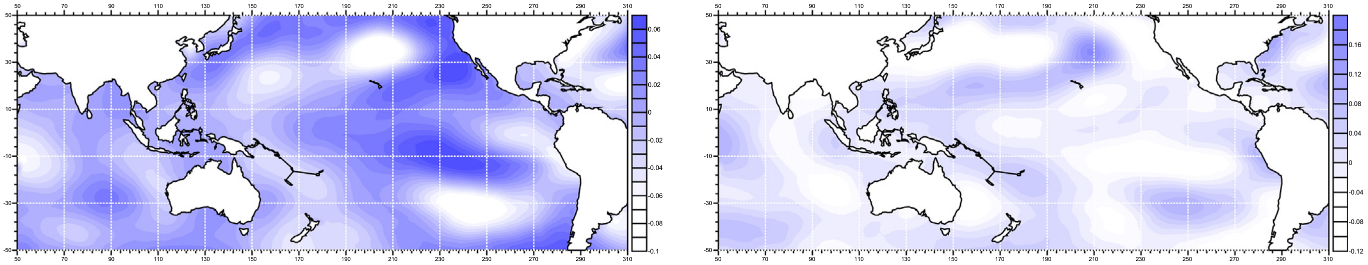

(a) MAR SST

(b) JUN SST

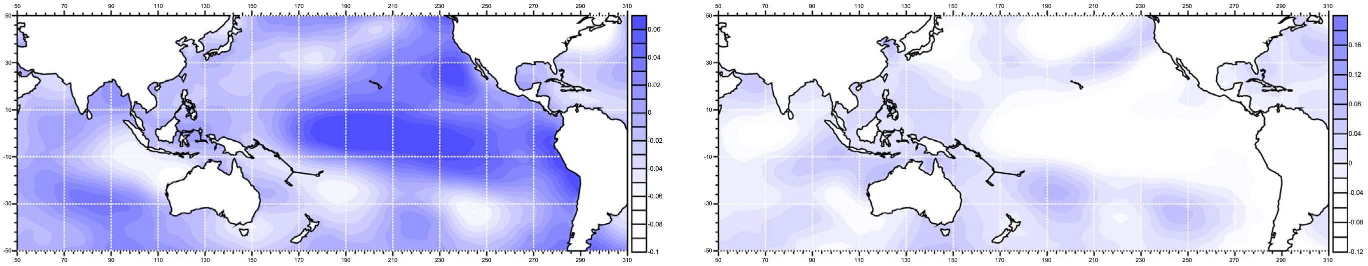

(c) SEP SST

(d) NOV SST

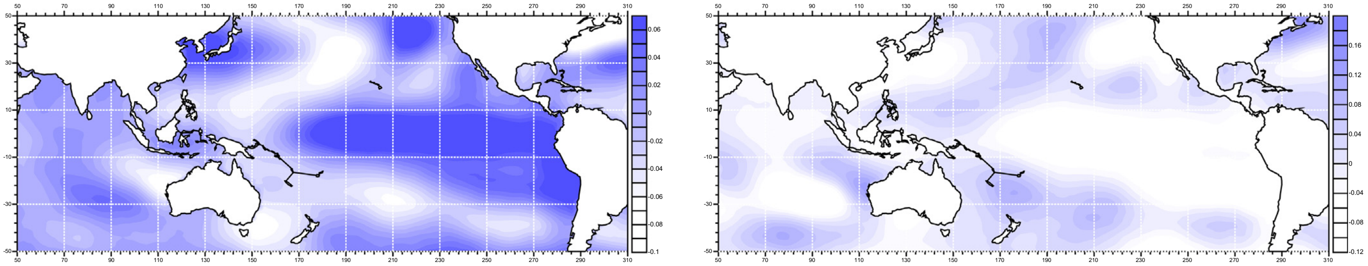

(a) MAR SST

(b) JUN SST

Fig. 9. Maps of SSTs of March to November regressed on to November leading mode for above (left) and below (right) normal extreme values only. The values of each grid of the maps are calculated using regression coefficients for Sea Surface Temperature (SST) of ERSST. v4 reconstructed field on the leading modes.

significant correlation with the TCI time series, indicating that increased and decreased frequency of tropical cyclones passing through the index area is associated with enhanced and suppressed REI variation as shown in Table 2. The leading modes in September exhibit the significant positive correlation with the tropical cyclone variability. This indicates that the leading modes in fall season, located in southern coastal area over South Korea, show significant positive correlation with the TCI.

3.3. Predictability of REI pattern

The cross-correlation coefficient between ENSO and each EOT/EOF mode was computed for the ONI, the MEI, and the SOI. As shown in Table 3, the ONI time series from June to November has the significant positive correlations with the leading EOT mode in November, while September EOT-1 exhibits the negative correlations with the ONI of June to September. The cross-correlation coefficient for the MEI time series similarly reflect the teleconnection between the EOT modes and ONI indices with mostly significant lagged responses three (September) to five (November) months in advance. The SOI has significant negative correlations with the November leading EOT at the same lead times of June to November, whereas the first EOT in September shows the positive correlation with SOI from the July to September. Generally, no significant correlation for the ENSO signal was detected during January to May reflecting the fact that relationships between the ENSO indicators and each EOT mode are usually not significant at this time of year. Also, the lagged responses are stronger in fall-winter season than in summer season since ENSO events are usually fully developed in boreal winter season. The outcomes from the above cross-correlation analysis indicate that the far reaching effects of the ENSO phenomena on the leading modes of REI in South Korea are detectable with up to five months lead times. Additionally, the leading EOF modes also show significant lagged correlation with ENSO remote forcing. The ONI, MEI, and SOI index show slightly lower correlation coefficients with the EOF modes compared with the EOT modes, but both correlation results show a similar seasonal cycle. The IOD is also associated with EOT/EOF

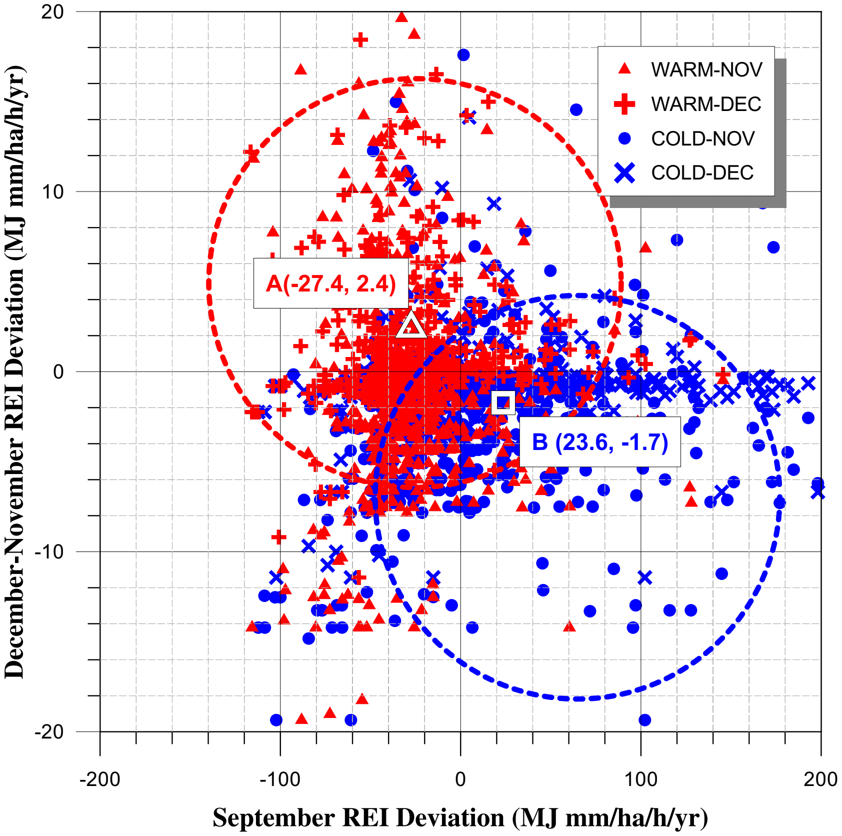

Fig. 10. The comparison of standardized indices for below (above) normal REI anomalies in September and above (below) normal REI in November–December during the warm (cold) phase of ENSO events using the monthly time series.

modes of REI variability in South Korea. In Table 3, the IOD indicator time series from June to September has the negative correlations with the leading EOT modes in September, while December DMI indices show the positive lagged correlation with September to December EOT modes at shorter lead times of lag-3. Also, the cross-correlation coefficients for the EOF modes similarly reflect the teleconnection between the EOT modes and IOD indices with mostly significant lagged responses two to three months in advance.

In addition to the cross-correlation analysis, the Pacific and Indian Ocean SSTs based on the ERSST.v4 dataset are regressed onto the leading modes with varying lead times to identify potential sources of predictability for monthly REI patterns. As shown in Figs. 7 and 8, the above lag regressions of the Pacific Ocean SSTs onto two leading modes, e.g., September and November EOT-1, demonstrate that the leading modes show notable lagged and concurrent regression with strong ENSO signals over the equatorial Pacific. The September lag-l regression, which regresses SSTs from previous months onto September EOT-1, shows noticeable predictability from the Pacific Ocean SST with negative regression coefficients decreasing as the lag increases. Significant lagged regression signals continue until months prior to June at lag-3, and then the Pacific SST-related REI signals tend to be disappear. Also, the November lag-l to lag-5 regression representing regression June to October SSTs onto November EOT-1, shows potential predictability by the tropical thermal forcing with positive regression coefficients. The significant positive signals extend to months prior to June at lag-5, and then do not exhibit during January to May. The spatial outlook of lag regression map indicates that the leading modes of the fall and winter REI patterns in South Korea provide a source of predictability induced by fluctuation of the Pacific Ocean SST. Despite noise in SST-REI relationship, the potential predictability sources analyzed above may provide a promising way for prediction of monthly REI variation.

In November, there is an asymmetric tendency in the ENSO-EOT modes relationship. The lagged and concurrent SST regressions onto the leading EOT-1 for above normal and below normal REI anomaly in November account for the aforementioned asymmetric tendency as shown in Fig. 9. These suggest that the potential predictability of very high extremes in November from Pacific SSTs is higher than that of very low November extremes. The lower predictability of January–May leading EOTs is attributed to weaker SST-REI relationships in this time of year. The potential sources of climate predictability extend to the EOF modes and consequently these findings indicate important implications for the seasonal forecasting the major hydrologic extremes.

3.4. Discussions

The EOT decomposition and cross-correlation analysis described in the previous section demonstrate that leading mode in September has a negative correlation with the tropical thermal forcing over Pacific Ocean, while that of November–December shows a positive response to the coupled ocean-atmosphere tropical SST variability. In other words, during the warm ENSO years below normal REI anomalies are observed in September, while above normal REI departures are observed in November–December. For the cold phase years, contrastingly, the REI anomalies in September show predominant positive departure in comparison with that of the non-event year, while negative anomalies are shown in November–December. Fig. 10 illustrates the comparison of standardized indices for below (above) normal REI in September and above (below) normal REI in November–December during the warm (cold) event years using the monthly data. The scatterplots for the warm phase are mostly distributed in the upper left part, while those for the cold phase are oppositely distributed in lower right part. These noticeable distribution patterns for both extreme phases suggest the opposite tendency of low and high anomalies in September and

November–December with respect to each extreme event. Taking into account that precipitation variability plays an important role in calculating the REI values, the findings from the above analyses are in general agreement with those reported by Lee and Julien (2016) who investigated the ENSO-precipitation teleconnection showing below normal precipitation anomaly during early fall season and above normal precipitation anomaly in late fall to winter season in association with the extreme phase of ENSO forcing.

The physical mechanisms behind the far reaching effects of the tropical ENSO forcing on the mid-latitude hydroclimatic variables are difficult to construct in general. The Pacific-East Asia (PEA) teleconnection, which was investigated by Wang et al. (2000), is a remote climatic link system of the SST anomalies over the central equatorial Pacific Ocean and the East Asian climatic variability during the ENSO event years. From the perspective of the cyclone and anticyclone over the WNP, the systematic configuration of the PEA teleconnection is considered as the lower tropospheric vorticity wave generated over the tropical Pacific Ocean with west-poleward shift against the westerly jet stream. They indicated that the WNP anomalous winds predominantly prevail and persist during late fall through ensuing winter of the ENSO event years, modulating precipitation-based hydrologic variabilities over East Asia by an enhanced or suppressed winter monsoon. These features affect the amplification or depression of fall-winter hydrologic variables in the ENSO event years. As a result, above or below normal variable departures are observed during fall-winter season of the extreme phase of ENSO phenomena throughout South Korea.

The overall results of these present analyses are in general agreement with those of several recent studies regarding the climatic impacts of the extreme phase of ENSO on hydroclimatic variables over South Korea in terms of ENSO-related signals for hydrologic variable such as precipitation and streamflow patterns. Cha et al. (1999) examined the teleconnection between the remote ENSO forcing and Korean climate such as precipitation, atmospheric circulation, temperature, and so on, and revealed that the tropical ENSO forcing has a dominant impact on fluctuation of seasonal precipitation over South Korea modulating enhancement of its magnitude in winter. In addition, from a viewpoint of ENSO-REI signal seasons illustrated in the cross-correlation analysis for the leading modes, the negative correlation in September is fairly coincident with the finding by Shin (2002) representing the suppression of early fall precipitation during the warm extreme event years. Therefore it is apparent that the findings from this presented study here are considered as an additional confirmation of aforementioned climatic far reaching effects of the large scale CIs on hydrologic parameter variability in South Korea. Consequently, in the light of the preceding discussions, the overall outcomes from the present analyses provide further confirmative evidence of the significant climatic teleconnection between the large scale CIs and hydroclimatic variability over mid-latitude.

4. Summary and conclusions

In the present study, we applied an empirical orthogonal teleconnection (EOT) and function (EOF) decomposition techniques to rainfall erosivity variability in order to examine remote impacts of large scale climate indices on hydrologic variables over South Korea. Also, we demonstrated predictability for hydrologic parameters by the tropical SST data on a monthly basis using cross-correlation and lag regression analysis for the leading modes and the ENSO and regional climate indicators.

The findings form this analyses are outlined as follows: (1) As shown in Fig. 4 based on the EOT/EOF analyses, the EOT leading modes explains more variance in REI variability than the leading EOF time series. Also, the spatiotemporal features of the REI variability over South Korea represent northern inland mode during summer and southern coastal mode in winter with mostly increasing and interdecadal timescales; (2) According to the statistical correlation results, the ONI and MEI time series have the significant negative correlations with the leading modes in September, whereas the leading modes in November and December exhibit the positive correlation with the tropical Pacific SST. The SOI shows significant positive (negative) correlations with the first modes during September (November–December). The three ENSO indicators generally show slightly higher correlation coefficients with the EOTs modes compared with the EOF modes, but both correlation results show a similar seasonal cycle. Also, the Indian Ocean dipole is identified as a driver for REI variability in November with positive correlation. As a result of correlation analysis between the leading modes and the local atmospheric circulation climate indices, the leading modes in December exhibit the negative correlation with the monsoon variability over western North Pacific, while the September leading modes show the positive correlation with the tropical cyclone variability; (3) From the results of cross-correlation and lag regression analyses, the leading modes in September and November have predictability up to five month lead time from the tropical Pacific SSTs. Also, the potential predictability from the tropical Pacific SSTs for very high extremes in November is higher than that of very low extremes.

References

Ashok, K., Guan, Z., Yamagata, T., 2001. Impact of the Indian Ocean dipole on the relationship between the Indian monsoon rainfall and ENSO. Geophys. Res. Lett. 28, 4499–4502.

Ashok, K., Guan, Z., Yamagata, T., 2003. Influence of the Indian Ocean dipole on the Australian winter rainfall. Geophys. Res. Lett. 30, 1821.

Biasutti, M., Seager, R., 2015. Projected changes in US rainfall erosivity. Hydrol. Earth Syst. Sci. 19, 2945–2961.

Bradley, R.S., Diaz, H.F., Kiladis, G.N., Eischeid, J.K., 1987. ENSO signal in continental temperature and precipitation records. Nature 327, 487–501.

Cayan, D.R., Peterson, D.H., 1989. The influence of North Pacific atmospheric circulation on streamflow in the West. In: Aspects of Climate Variability in the Pacific and the Western Americas. Amer. Geophys. Union, Monogr. Vol. 55. pp. 375–397.

Cayan, D.R., Webb, R.H., 1992. El Niño/Southern Oscillation and streamflow in the Western United States. In: Diaz, H.F., Markgraf, V. (Eds.), El Niño: Historical and Paleoclimatic Aspects of the Southern Oscillation. Cambridge University Press, pp. 29–68.

Cha, E.J., 2007. El Niño-Southern Oscillation, Indian Ocean dipole mode, a relationship between the two phenomena, and their impact on the climate over the Korean Peninsula. J. Korean Earth Sci. Soc. 28 (1), 35–44.

Cha, E.J., Jhun, J.G., Chung, H.S., 1999. A study on characteristics of climate in South Korea for El Niño/La Niña years. J. KMS 35 (1), 99–117.

Chandimala, J., Zubair, L., 2007. Predictability of streamflow and rainfall based on ENSO for water resources management in Sri Lanka. J. Hydrol. 335, 303–312.

Diaz, H.F., Kiladis, G.N., 1993. El Niño/Southern Oscillation and streamflow in the Western United States. In: Diaz, H.F., Markgraf, V. (Eds.), El Nitio: Historical and Paleoclimatic Aspects of the Southern Oscillation. Cambridge University Press, pp. 8–28.

Douglas, A.E., Englehart, P.J., 1981. On a statistical relationship between autumn rainfall in the central equatorial pacific and subsequent winter precipitation in Florida. Mon. Weather Rev. 109, 2377–2382.

Guttman, N.B., 1998. Comparing the Palmer drought index and the standardized precipitation index. J. Am. Water Resour. Assoc. 34 (1), 113–121.

Hoomehr, S., Schwartz, J., Yoder, D.C., 2015. Potenial change in rainfall erosivity under GCM climate change scenarios for the southern Appalachian region, USA. Catena 136, 141–151.

Huang, B., Banzon, V.F., Freeman, E., Lawrimore, J., Liu, W., Peterson, T.C., Smith, T.M., Thorne, P.W., Woodruff, S.D., Zhang, H.M., 2014. Extended reconstructed sea surface temperature version 4 (ERSST.v4): Part I. Upgrades and intercomparisons. J. Clim. http://dx.doi.org/10.1175/JCLI-D-14-00006.1.

Jung, P., Ko, M., Im, J., Um, K., Choi, D., 1998. Rainfall erosion factor for estimating soil loss (in Korean). J. Korean Soc. Soil Sci. Fert. 16 (2), 112–118.

Kahya, E., Dracup, J.A., 1994. The influences of type 1 El Niño and La Niña events on streamflows in the Pacific southwest of the United States. J. Clim. 7, 965–976.

Kiladis, G.N., Diaz, H.F., 1989. Global climatic anomalies associated with extremes in the Southern Oscillation. J. Clim. 2, 1069–1090.

Kim, M.K., Kang, I.S., Park, C.K., Kim, K.M., 2004. Super ensemble prediction of regional precipitation over Korea. Int. J. Climatol. 24, 777–790.

King, A.D., Klingaman, N.P., Alexander, L.V., Donat, M.G., Jourdain, N.C., Maher, P., 2014. Extreme rainfall variability in Australia: patterns, drivers, and predictability. J. Clim. 27, 6035–6050.

Knapp, K.R., Kruk, M.C., Levinson, D.H., Diamond, H.J., Neumann, C.J., 2010. The international best track archive for climate stewardship (ibtracs): unifying tropical cyclone best track data. Bull. Am. Meteorol. Soc. 91, 363–376.

Lee, J., Heo, J., 2011. Evaluation of estimation methods for rainfall erosivity based on annual precipitation in Korea. J. Hydrol. 409, 30–48.

Lee, J.H., Julien, P.Y., 2015. ENSO impacts on temperature over South Korea. Int. J. Climatol. 10, 1002/4581.

Lee, J.H., Julien, P.Y., 2016. Teleconnections of the ENSO and South Korean precipitation patterns. J. Hydrol. 534, 237–250.

Lee, J.H., Julien, P.Y., 2017. Influence of the El Niño/southern oscillation on South Korean streamflow variability. Hydrol. Process. http://dx.doi.org/10.1002/hyp.11168.

McKee, T.B., Doesken, N.J., Kleist, J., 1993. The relationship of drought frequency and duration to time series. In: 8th Conference on Applied Climatology, Anaheim, CA 1993, pp. 179–187.

Mohammadi, M., 2015. Rainfall trends and their impacts on soil erosion in north watersheds of Iran. J. Nov. Appl. Sci. 4 (6), 674–681.

Mondal, A., Khare, D., Kundu, S., 2016. Change in rainfall Erosivity in the past and future due to climate change in the central part of India. Int. Soil Water Conserv. Res. 4 (3), 186–194.

National Institute of Agricultural Sciences, 2005. Assessment of soil erosion potential in Korea. In: Pamphlet. No. 11-1390093-020109-01.

Nearing, M.A., 2001. Potential changes in rainfall erosivity in the U.S. with climate change during the 21st century. J. Soil Water Conserv. 56 (3), 229–232.

Nearing, M.A., Pruski, F.F., O'Neal, M.R., 2004. Expected climate change impacts on soil erosion rates: a review. J. Soil Water Conserv. 59 (1), 43–50.

Panagos, P., Borrelli, P., Meusburger, K., Yu, B., Klik, A., Lim, K.J., Yang, J.E., Ni, J., Miao, C., Chattopadhyay, N., Sadeghi, S.H.R., Hazbavi, Z., Zabihi, M., Larionov, G.A., Krasnov, S.F., Gorobets, A.V., Levi, Y., Erpul, G., Birkel, C., Hoyos, N., Naipal, V., Oliveira, P.T.S., Bonilla, C.A., Meddi, M., Nel, W., Al Dashti, H., Boni, M., Diodato, N., Van Oost, K., Nearing, M., Ballabio, C., 2017. Global rainfall erosivity assessment based on high-temporal resolution rainfall records. Nat. Sci. Rep. 7, 4175.

Park, J., Woo, H., Pyun, C., Kim, K., 2000. A study of distribution of rainfall erosivity in USLE/RUSLE for estimation of soil loss (in Korean). J. Korean Water Res. Assoc. 33 (5), 603–610.

Park, C., Sonn, Y., Hyun, B., Song, K., Chun, H., Moon, Y., Yun, S., 2011. The re-determination of USLE rainfall erosion factor for estimation of soil loss at Korea. Korean J. Soil Sci. Fert. 44 (6), 977–982.

Plangoen, P., Babel, M.S., 2014. Projected rainfall erosivity changes under future climate in the upper nan watershed, Thailand. J. Earth Sci. Clim. Change 5 (242). http://dx.doi.org/10.4172/2157-7617.1000242.

Plangoen, P., Babel, M.S., Clemente, R.S., Shrestha, S., Tripathi, N.K., 2013. Simulating the impact of future land use and climate change on soil erosion and deposition in the Mae Nam nan sub-catchment, Thailand. Sustainability 5, 3244–3274.

Price, C., Stone, L., Huppert, A., Rajagopalan, B., Alpert, P., 1998. A possible link between El Niño and precipitation in Israel. Geophys. Res. Lett. 25, 3963–3966.

Rasmusson, E.M., Wallace, J.M., 1983. Meteorological aspects of the El Niño/southern oscillation. Science 222, 1195–1202.

Redmond, K.T., Koch, R.W., 1991. Surface climate and streamflow variability in the western United States and their relationship to large circulation indices. Water Resour. Res. 27 (9), 2381–2399, 1991.

Renard, K.G., Foster, G.R., Weesies, G.A., McCool, D.K., Yode, D.C., 1997. Predicting soil erosion by water: a guide to conservation planning with the Revised Universal Soil Loss Equation, RUSLE. In: Agriculture Handbook, No.703. USDA.

Risal, A., Bhattarai, R., Kum, D., Park, Y.S., Yang, J.E., Lim, K.J., 2016. Application of web ERosivity module (WERM) for estimation of annual and monthly R factor in Korea. Catena 147, 225–237.

Ropelewski, C.F., Halpert, M.S., 1989. Precipitation patterns associated with the high index phase of the southern oscillation. J. Clim. 2, 268–284.

Saji, N.H., Goswami, B.N., Vinayachandran, P.N., Yamagata, T., 1999. A dipole mode in the tropical Indian Ocean. Nature 401, 360–363.

Shin, H.S., 2002. Do El Niño and La Niña have influences on South Korean hydrologic properties? In: Proceedings of the 2002 Annual Conference. Japan Society of Hydrology and Water Resourcespp. 276–282.

Shiono, T., Ogawa, S., Miyamoto, T., Kameyama, K., 2013. Expected Impacts of Climate Change on Rainfall Erosivity of Farmlands in Japan.

Shukla, J., Paolino, D.A., 1983. The southern oscillation and long-range forecasting of summer monsoon rainfall over India. Mon. Weather Rev. 111, 1830–1837.

Smith, I.N., 2004. An assessment of recent trends in Australian rainfall. Aust. Meteor. Mag. 53, 163–173.

Van den Dool, H.M., Saha, S., Johansson, Å., 2000. Empirical orthogonal teleconnections. J. Clim. 13, 1421–1435.

Walker, G.T., 1923. Correlation in seasonal variations of weather, V III, a preliminary study of world weather. Mem. Indian Meteorol. Dep. 24, 75–131.

Wang, B., Fan, Z., 1999. Choice of South Asian summer monsoon indices. Bull. Am. Meteorol. Soc. 80, 629–638.

Wang, B., Wu, R., Fu, X., 2000. Pacific–East Asian teleconnection: how does ENSO affect East Asian climate. J. Clim. 13, 1517–1536.

Wang, B., Wu, R., Li, J., Liu, J., Chang, C., Ding, Y., Wu, G., 2008. How to measure the strength of the East Asian Summer Monsoon. J. Clim. 1175.

Wischmeier, W.H., Smith, D.D., 1978. Predicting rainfall erosion losses – a guide to conservation planning. In: USDA Agric. Handbook, No. 537, Washington, D.C.

Yang, D., Kanae, S., Oki, T., Koike, T., Musiake, K., 2003. Global potential soil erosion with reference to land use and climate changes. Hydrol. Process. 17, 2913–2928.

Yang, X., Bofu, Y., Xiaojin, X., 2015. Predicting changes of rainfall erosivity and hillslope erosion risk across greater Sydney region, Australia. Int. J. Geospat. Environ. Res. 2 (1), 2. http://dc.uwm.edu/ijger/vol2/iss1/2.

Zhang, G.H., Nearing, M.A., Liu, B.Y., 2005. Trans. ASAE 48 (2), 511–517.